Oxidation effect on optical properties of integrated waveguides based on porous silicon layers at mid-infrared wavelength

Abdallah Jaafar, Sofiane Meziani, Abdelali Hammouti, Parastesh Pirasteh, Nathalie Lorrain, Loïc Bodiou, Mohammed Guendouz, Joël Charrier

Oxidation effect on optical properties of integrated waveguides based on porous silicon layers at mid-infrared wavelength

Authors

A. Jaafar, S. Meziani, A. Hammouti, P. Pirasteh, N. Lorrain, L. Bodiou, M. Guendouz and J. Charrier

Institut Foton, Université de Rennes, CNRS, - UMR 6082, F-22305 Lannion, France

Abstract

Integrated sensors based on guided optical devices can efficiently and selectively detect molecules in the mid-infrared (mid-IR) spectral range, exploiting the vibrational and rotational modes of these molecules at these wavelengths. In this work, a ridge waveguide based on porous silicon (PSi) layers was developed by electrochemical etching followed by a photolithographic process. The ridge waveguide is capable of propagating light in the mid-IR range (3.90 - 4.35 µm) with optical losses of approximately 10 dB/cm. An oxidation study was performed to stabilize the porous structure and identify the optimal oxidation degree, that allow mid-IR light to propagate in a ridge waveguide based on PSi material for sensing application. The results showed that the ridge waveguide remains capable of propagating light after undergoing partial oxidation at 300 °C and 600 °C (15% and 36 % of the oxidation degree respectively) with optical losses of around 30 dB/cm and 60 dB/cm at the wavelength of 4.1 µm, respectively.

Keywords

Porous Silicon layers, oxidation treatment, refractive index, ridge waveguide, optical losses, Mid-Infrared.

1. Introduction

Miniaturized optical sensor devices based on photonic integrated circuits (PICs) have been extensively investigated in the last years due to their advantages such as compactness, low cost, high speed, high sensitivity, low limit of detection and high selectivity that are not affected by other environmental factors such as thermal, chemical or mechanical effects [1]. Over the past decade, silicon photonics for the near-infrared (NIR) range spectral have attracted a great deal of interest from researchers [2, 3]. Recent advances offer the possibility of extending the operational wavelength to the mid-IR, which is considered as a key enabling technology for new generation of sensing applications [4-6]. This is because the mid-IR range (2 - 20 µm) is the vibrational spectral region of organic and inorganic compounds present in water, air and environment [7].

Porous silicon (PSi) material has attracted great scientific and practical interest in recent years due to their special physical, chemical and optical characteristics [8, 9]. PSi material is widely studied in several applications such as microelectronics [10], photovoltaic [11] and biosensor [12]. Porous structures are of specific interest for optical applications, particularly for optical sensing, because they have a high specific internal surface area and a tunable porosity and therefore a tunable refractive index that allow photonics engineering [13]. The fabrication of an optical waveguide based on PSi layers was initiated in the 1990s, and their optical characterization was studied from UV-visible to near-infrared spectral range [14-18]. Indeed, more recent works have extended these studies to the

mid-infrared region with bulk materials [19, 20], while our work describes these components made from porous material.

Sensitivity and limit of detection are used to evaluate the performance of an optical sensor. These parameters strongly depend on the interaction between the target molecules and the propagated light. Two different detection methods are possible namely surface and volume detection. In the case of surface detection scheme, the optical waveguide is based on a bulk material and the propagating light only interacts through its the evanescent part with the molecules that are present close to the waveguide surface [19, 21]. Volume detection can be implemented with porous materials-based waveguiding structure. In such case, detected molecules can penetrate into the pores and therefore the propagating light not only interacts with targeted molecules through the evanescent wave but also through the part of the field in the guiding and cladding layers. This results in a higher interaction and significant improvement in the ability to detect a very small number of molecules with high sensitivity [17, 22].

However, the porous structure is unstable at room temperature due to the high internal surface area, resulting in contamination and native oxidation of the PSi surface [23]. The stabilization of the PSi structures is usually achieved by performing an oxidation process [24], because silica (SiO_2) has a good chemical stability. Moreover, silica has strong absorption in the mid-IR range, which is the main problem in thermally stabilized structure of a waveguide based on PSi material operating at mid-IR wavelengths. Optimizing the oxidation degree by controlling the oxidation treatment for this type of optical waveguide is necessary to enable high performance in optical sensing applications.

In this work, a ridge waveguide based on PSi layers (guiding and cladding layers) was developed by electrochemical etching followed by a photolithographic process. Then this structure was stabilized under thermal oxidation treatment [25]. The main objective of this paper is to determine the optimal oxidation degree for a ridge waveguide based on PSi material that allow light to propagate in the mid-IR wavelength range at around 4.3 µm. The influence of the oxidation treatment on the complex refractive indices of the porous single layers was determined, and the optical losses measurement of a PSi ridge waveguide as a function of the oxidation degree was performed.

2. Experimental conditions

The PSi layers were fabricated at room temperature by the electrochemical etching of ~ 3.5 cm^2 surface area of a heavily B-doped p-type (100) silicon substrate with a 5 mΩ.cm resistivity. Four samples were prepared using various current densities ranging from 30 to 100 mA/cm^2 (Table 1).

Sample	**Current density (mA/cm^2)**	**Thickness (µm)**	**Etching rate (nm/s)**
S1	30	5	21
S2	50	5	31
S3	80	4.8	43
S4	100	5	50

Table 1: List of parameters used for the development of the porous silicon layers.

The electrolyte is composed of a mixture of hydrofluoric acid (50 %), ethanol (≥ 99.98 %) and deionized water (18 MΩ) in a 2-2-1 ratio. Thickness of PSi layers was controlled by adjusting the etching time and was further measured using scanning electron microscopy (SEM) by imaging the cross-section of the sample as shown in Figure 1, as well as the columnar pore structure, perpendicular to the silicon surface.

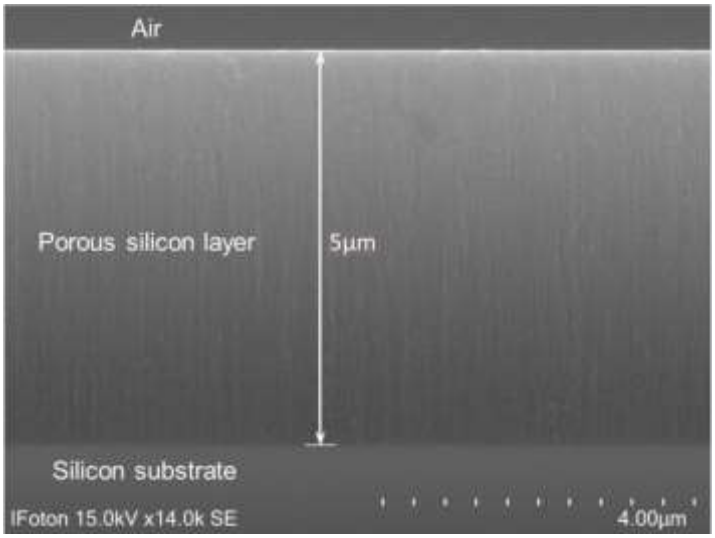

Figure 1: SEM cross-sectional image of the as-prepared PSi layer prepared with 50 mA/cm^2.

Mid-IR reflectance spectra were recorded with a Perkin Elmer Spectrum 100 FTIR spectrometer from 2.5 to 8 µm with a resolution of 1 cm^{-1}. Measurement calibration was performed using a gold mirror with a calibrated 97.5% reflection between 2.5 and 8 µm. The calibration protocol of the spectrometer takes into account absorption from laboratory ambient environment, in particular, absorption fringes of CO_2, water vapor and methane. From reflectance spectra, the refractive index for each of the fabricated single PSi layers was deduced by fitting experimental spectral fringes using the effective medium theory, Bruggeman model [26]. Previous studies have shown that the porous structure of the PSi layer can be stabilized at 300 °C before applying a high oxidation temperature [27]. A partial oxidation step should be carried out for temperatures above 440 °C [28], and complete oxidation can be achieved at 850 °C [29]. For this reason, the oxidation study of the all single layers in this work (samples S1, S2, S3 and S4) was carried out in air at three different temperatures and times: a pre-oxidation step at 300 °C for one hour, a partial oxidation at 600 °C for 30 minutes after the pre-oxidation step, and a complete oxidation at 900 °C for 30 minutes after the two previous steps (figure 2). We note that for the oxidation study, each individual sample (S1, S2, S3 and S4) was cut into four pieces, one piece was used as a reference sample (unoxidized) and the other three pieces were studied at different oxidation treatments.

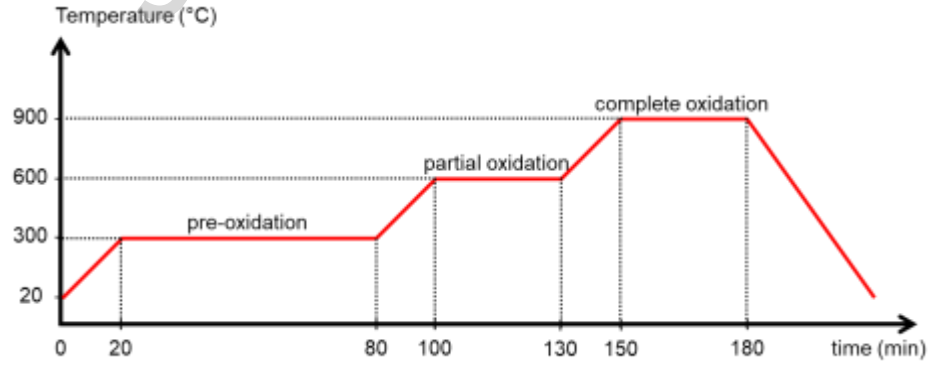

Figure 2: Temperature diagram for oxidation treatment of PSi layers.

FTIR reflectance spectra have also been performed on the four samples after each studied oxidation treatment (pre-oxidation, partial oxidation and complete oxidation). The porosity, the refractive index and the oxidation degree of the PSi layer were deduced from the spectra analyses.

Then, a planar waveguide formed by two consecutive PSi layers of different porosities was also developed by electrochemical anodization using two different current densities: a guiding layer with 50 mA/cm^2 and a cladding layer with 100 mA/cm^2. These two layers were preceded by a very thin PSi layer with a low porosity (1 mA/cm^2). The presence of this PSi barrier layer is necessary to prevent photoresist infiltration into the pores during the photolithographic process [17]. Ridge waveguide (figure 3) was obtained using a standard photolithographic process followed by a dry etching step (20 sccm CHF_3, RIE/ICP power: 25/400 W at 5 mTorr). ~~An optical bench and a Mid-IR laser were used to observe the light propagation and to measure the optical losses of the ridge waveguide. These optical losses were measured as a function of oxidation treatment, after each oxidation step.~~ An optical characterization was carried out on the PSi ridge waveguide using the mid-IR bench, with a tunable QCL emitting from λ = 3.9 to 4.6 µm (*MIRCAT, Daylight Solutions*). The input light was coupled into the waveguide by injecting it into an optical fiber, so no light polarization was used in this work. The output light from the waveguide was collimated towards a detector (*DSS-PSE020TC, Horiba*) using a mid-IR objective lens. These optical characterizations were carried out to observe light propagation and to measure the optical losses of the ridge waveguide. These optical losses were measured as a function of oxidation treatment, after each oxidation step. It should be noted that the optical losses were performed using 11 waveguides of different lengths (from 1.25 to 1.75 cm) in order to determine optical losses using the Cut-Back method.

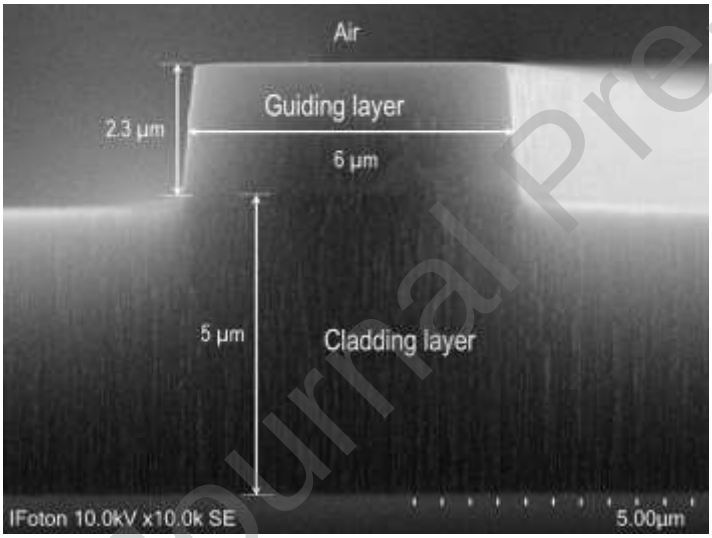

Figure 3: SEM cross-sectional image of the ridge waveguide designed using the photolithography process: guiding layer with current density of 50 mA/cm^2 and cladding layer with current density of 100 mA/cm^2.

3. Results and discussion

3.1. Single PSi layers

The effect of the oxidation treatment on the PSi single layers is shown schematically in Figure 4. The oxidation changes pore diameter, Si crystallite size, PSi layer thickness, specific surface area and consequently porosity (therefore refractive index) of the PSi layer, due to the insertion of oxygen atoms into the pores.

The oxidation of the PSi layer can be described by the oxidation degree (τ_{ox}), which vary between the values 0 and 1, and it can be expressed as the following equation: $\tau_{ox} = C/C_{Si}$ with C, the volume

fraction of Si transformed into SiO_2 and C_{Si}, the initial volume fraction of silicon. For the as-prepared PSi layer, the oxidation degree is equal to 0 (Figure 4-a); after total oxidation it is equal to 1 (Figure 4-c); and after partial oxidation the oxidation degree can vary between 0 and 1 (Figure 4-b). It has been demonstrated that the insertion of oxygen atoms between and onto the silicon crystallites has allowed an expansion effect on the pores of the PSi layer and the expansion of their thickness after total oxidation for photonic integrated circuit based on PSi layers [30, 31]. However the pores did not collapse because of the initial porosity which was more important than the volume expansion and the structure was always open on the surface and still porous.

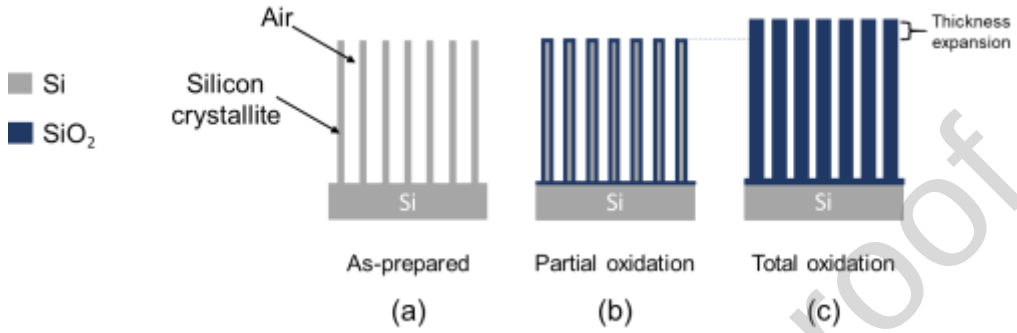

Figure 4: Schematic cross section of the PSi layer: (a) as prepared, (b) partially and (c) completely oxidized (porous silica).

Firstly, the PSi single layers were characterized as a function of oxidation degree by FTIR spectroscopy. Figure 5 illustrates the fit of the experimental (red curves) and theoretical (blue curves) spectra in the mid-IR spectral range for the PSi layer grown at 50 mA/cm^2 (sample S2) for different oxidation degrees. Fabry-Perrot interference fringes are caused by the air-PSi and PSi-Si substrate interfaces. Note that the absorption peak around 4.8 µm in Figure 5-a represents the Si-H vibration mode [32].

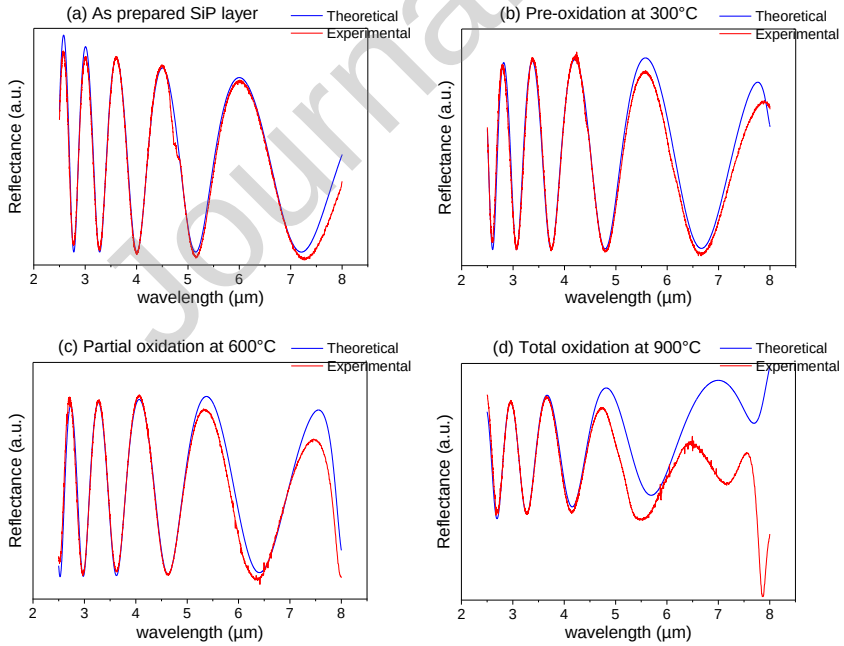

Figure 5: Fitting experimental and theoretical spectra in the mid-IR spectral range of the PSi layer developed at 50 mA/cm^2: (a) as-prepared, (b) pre-oxidized, (c) partially and (d) completely oxidized.

As mentioned previously, the PSi layers are transparent up to 8 µm due to the mid-IR optical properties of silicon. After pre-oxidation at 300 °C for one hour (Figure 5-b), the deformation of the interference fringe began at the wavelength around 7 µm, indicating the absorption of silica formed on the surface of the pores. After partial oxidation at 600 °C for 30 minutes (Figure 5-c), the thickness of the SiO_2 layer increases, and then the absorption of silica takes place at a wavelength around 6 µm. Finally, Figure 5-d illustrates the PSi layer completely oxidized after oxidation at 900 °C for 30 minutes, and thus the silica absorption dominates in this medium, reducing the transparency in the wavelength range of the PSi layer from 8 to around 5 µm. ~~Note that the high porosity (samples 2 and 4) was chosen in this work to avoid pore collapse after the oxidation treatment and to realize a volume detection mode.~~ Note that the porosity beyond 50 % was chosen in this work to avoid pore collapse after the oxidation treatment and to realize a volume detection mode.

The refractive index of the PSi layer was determined by fitting the calculated FTIR spectrum obtained using the transfer matrix method [33], to the experimental spectrum, knowing the thickness of the PSi layer determined by SEM observation. Note that the adjustment takes into account the absorption part $\mathrm{k(n)}$ of the refractive index of silica ($\mathrm{n_{SiO_2} = n_{real} + ik}$). Then the porosity and the oxidation degree of the layer was deduced using the Bruggeman model (Equation 1) [26, 34]. This model relates the effective refractive index of the layer n to the refractive index $\mathrm{n_i}$ of the different constituent i (air, silicon or silica) of the porous layer and their volume fraction $\mathrm{C_i}$, where $(\sum_i \mathrm{C_i})$ is equal to 1.

$$\sum_i C_i \frac{n_i^2(\lambda) - n^2(\lambda)}{n_i^2(\lambda) + 2n^2(\lambda)} = 0 \qquad (1)$$

Before the oxidation treatment (as-prepared sample; $\tau_{ox} = 0$), i component are: air and silicon. The volume fractions of air and silicon are represented as $\mathrm{C_{air}}$ and $\mathrm{C_{Si}}$, respectively. Consequently, the initial porosity $\mathrm{P_{ini}}$ of the PSi layer, i.e. the volume fraction of air ($\mathrm{C_{air}}$) can be described by the following equation:

$$P_{ini} = C_{air} = 1 - C_{Si} \qquad (2)$$

Thereby, both for the pre-oxidation and the partial oxidation treatment ($0 < \tau_{ox} < 1$), i component are: air, silicon and silica. In this case, the volume fraction of air, silicon and silica are represented as $\mathrm{C'_{air}}$, $\mathrm{C'_{Si}}$ and $\mathrm{C_{SiO_2}}$, respectively. Taking into account the expansion factor of silicon transformed into silica, which is equal to 2.27 [30], we can deduced $\mathrm{C'_{Si}}$, $\mathrm{C_{SiO_2}}$ and the porosity after pre- and partial-oxidation ($\mathrm{C'_{air}}$) by the following equations:

$$\mathrm{C'_{Si} = C_{Si} - C = C_{Si}\,(1 - \tau_{ox})} \qquad (3)$$

$$\mathrm{C_{SiO_2} = 2.27\,C = 2.27\,\tau_{ox}\,C_{Si}} \qquad (4)$$

$$\mathrm{C'_{air} = C_{air} - 1.27\,C = P_{ini} - 1.27\,\tau_{ox}\,C_{Si}} \qquad (5)$$

After total oxidation of PSi layer ($\tau_{ox} = 1$), i component are: air and silica, $\mathrm{C'_{air}}$ can be described by the following equation:

$$C'_{air} = 1 - C_{SiO_2} \qquad (6)$$

Table 2 reports the volume fractions of air (porosity) and silica deduced from the adjustment of reflectance spectra of the PSi layers (S1, S2, S3 and S4) prepared at different current densities before and after oxidation treatment. The thickness of the different samples measured by SEM is also mentioned.

	As-prepared		**Pre-oxidation**			**Partial oxidation**			**Complete oxidation**		
Sample	C_{air}	t_0 (µm)	C'_{air}	C_{SiO_2}	t_1 (µm)	C'_{air}	C_{SiO_2}	t_2 (µm)	C'_{air}	C_{SiO_2}	t_3 (µm)
S1	0.52	5.0	0.44	0.14	5.0	0.35	0.31	5.0	0.24	0.76	6.0
S2	0.60	5.0	0.52	0.14	5.0	0.42	0.31	5.0	0.28	0.72	5.7
S3	0.66	4.8	0.58	0.14	4.8	0.49	0.31	4.8	0.40	0.60	5.3
S4	0.73	5.0	0.66	0.14	5.0	0.56	0.31	5.0	0.54	0.46	5.4

Table 2: List of volume fractions of air and silica (C_i), the thickness (t_i) of PSi layers developed at various current densities and as a function of oxidation treatment. The standard deviation of thickness is equal to 0.1 µm, volume fractions of air is 1 % and of silica is 1 % and 2 % after pre-oxidation and partial oxidation, respectively.

The porosity of the PSi layers decreases with oxidation temperature, due to the decreased pore volume that is caused by the insertion of oxygen atoms into the pores of the PSi layer. The volume fraction of silica increases with temperature but is almost independent of the initial porosity (P_{ini}), for the cases of the pre-oxidation (C_{SiO_2}~ 0.14) and partial oxidation (C_{SiO_2}~ 0.31), demonstrating the homogeneity of the oxidation treatment method used in this work. In additional, after total oxidation, the volume fraction of silica decreases with increasing porosity due to the decrease in the amount of silicon in PSi.

The refractive index deduced from reflectance spectra analyses of the PSi layers at different current densities (S1, S2, S3 and S4) and oxidation treatment is plotted as a function of wavelength in Figure 6. These graphs show that the refractive index curves of PSi layers decrease with increasing current density and the oxidation treatment. Indeed, the volume fraction of air (porosity) increases with current density, and the volume fraction of silica (C_{SiO_2}) increases with oxidation treatment, respectively, leading to a decrease in the refractive index of the PSi layer. Knowing that the refractive index of silicon is higher than of air and silica. After the pre-oxidation step (figure 6-b), the refractive index of the PSi layers decreases with the oxidation treatment by around 0.1, due to the transformation of silicon into silica in the porous layers. Silica has a high absorption in the mid-IR, which increases with wavelength, and a low refractive index (n_{SiO_2}) ranging from 1.44 to 0.7 in the mid-IR wavelength range from 1.55 to 8 µm, respectively. After partial oxidation (figure 6-c), the amount of silica increases in the PSi layer and so the index decreases furthermore. Finally, after total oxidation (figure 6-d) the porous layer has become a silica porous layer and therefore the refractive index becomes very low (between n_{air} and n_{SiO_2} values). On the other hand, the refractive index is also higher in the near-IR than in the mid-IR, due to the wavelength-dependent optical properties of silicon and silica [35, 36].

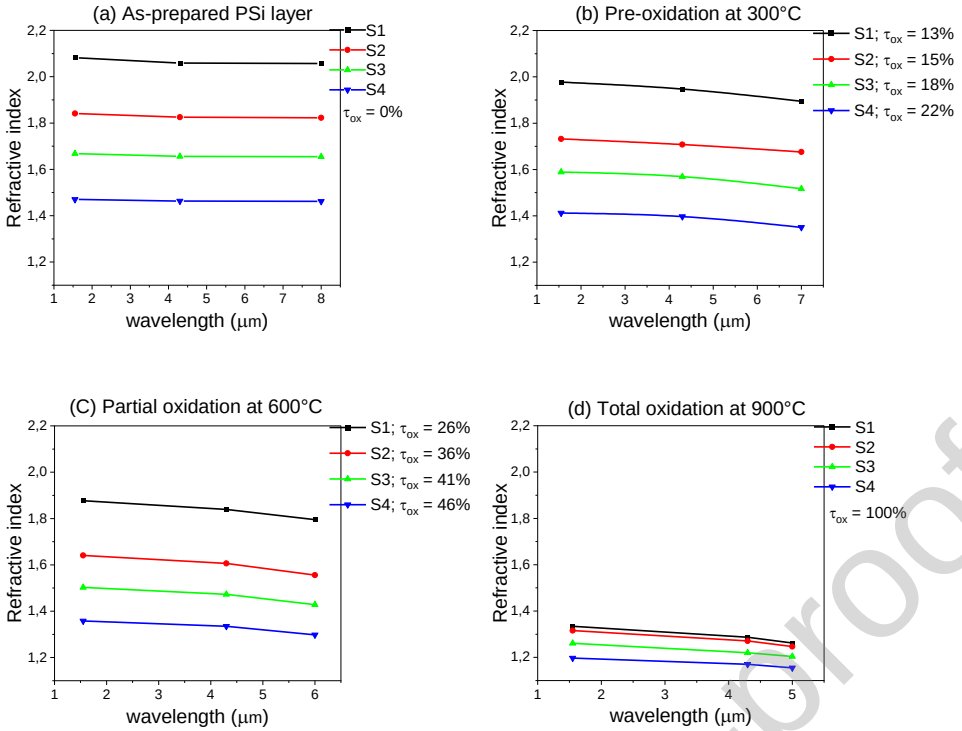

Figure 6: Refractive index dispersion for a PSi layer with different porosities and as a function of wavelength: (a) as-prepared, (b) pre-oxidized, (c) partially and (d) totally oxidized.

From the results in Table 2, the imaginary part of the complex refractive index $k(n)$ of an oxidized PSi layer can be estimated, $k(n)$ is related directly to the absorption loss of silica. Figure 7 shows the imaginary part $k(n)$ of silica in the mid-IR range as a function of oxidation treatment, for a PSi layer developed at 50 mA/cm^2 (sample S2). The curves increase with wavelength and oxidation treatment, due to the mid-IR optical properties of silica and the increase in the amount of silica in the PSi layers during the oxidation treatment, respectively. These results are correlated with the graphs in Figure 5-b, -c and -d, which explain how silica absorption greater than $k(n)$ ~ 5 E^{-4} can lead to deformation of the reflectance fringes.

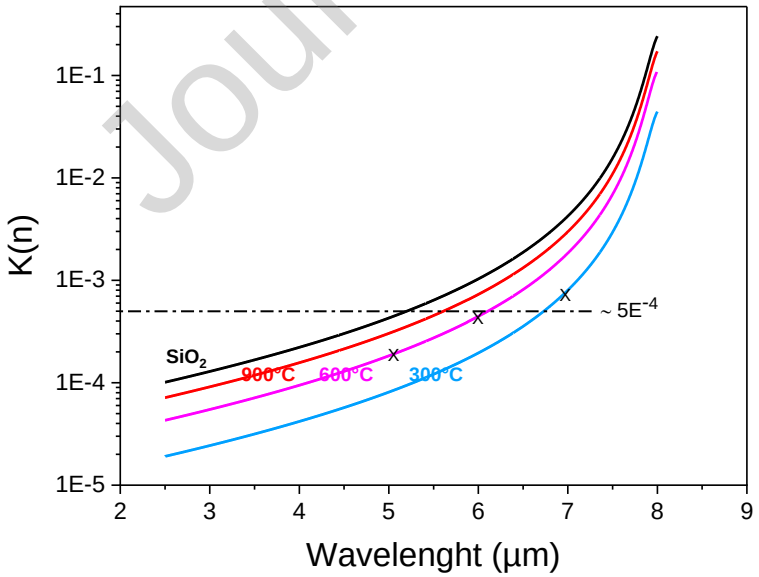

Figure 7: The imaginary part $k(n)$ of silica in the mid-IR as a function of oxidation treatment for a PSi layer developed at 50 mA/cm^2.

Figure 8-a shows that the oxidation degree of PSi layers after the oxidation treatment at 300 °C and 600 °C increases with temperature and initial porosity (P_{ini}). The latter can be explained by the decrease in the volume fraction of silicon (C_{Si}) with P_{ini} (equation 2), and by maintaining the volume fraction of silica nearly constant after pre- and partial-oxidation as a function of P_{ini} (Table 2), Therefore, in accordance with the equation $\tau_{ox} = C/C_{Si}$, the oxidation degree increases with P_{ini}.

The insertion of a large amount of oxygen between and on the Si crystallites leads to the expansion of the PSi layer thickness, which is also strongly dependent on initial porosity. In fact, after partial oxidation, the volume expansion of pores does not change the PSi layer thickness, it simply leads to a reduction of the average pore diameter and thus of the PSi layer porosity (C'_{air}), as indicated in Table 2. However, after complete oxidation, the volume expansion of pores is much larger, resulting in a decrease in porosity (C'_{air}) and an increase in the thickness of the PSi layer.

The PSi layer's expansion thickness was calculated by equation (7).

$$\Delta t = \frac{t_{ox} - t}{t} \qquad (7)$$

With Δt, the expansion thickness of the PSi layer; t, the thickness of the as-prepared PSi layers and t_{ox}, the thickness of the layers after complete oxidation.

Figure 8-b reports the expansion thickness of the PSi layer as a function of the initial porosity in the case of a complete oxidation. This figure shows that the expansion thickness (Δt) of PSi layer after complete oxidation decreases with P_{ini}. In the case of high initial porosity, the initial pore diameter is larger than that of low porosity; thus, the pore expansion could be dominated by the pore diameter rather than an expansion of the layer thickness.

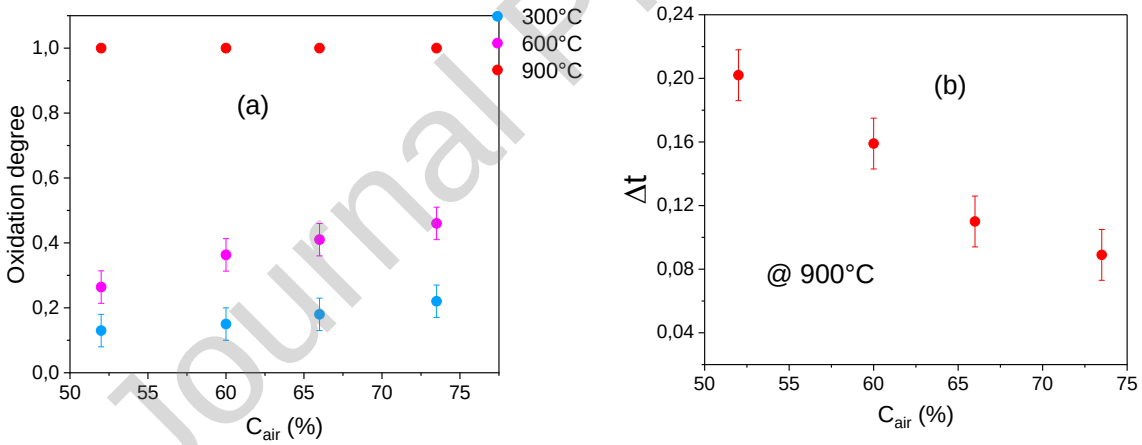

Figure 8: Oxidation degree as a function of initial porosity (P_{ini}) and oxidized temperature (a). Thickness expansion of the PSi layer after full oxidation as a function of initial porosity (b).

3.2. PSi ridge waveguide

A PSi bilayer structure preceded by a thin technological barrier for the subsequent photolithographic process was characterized by FTIR spectroscopy to determine the refractive index and porosity of each layer. The refractive index of the guiding layer prepared by applying a current density of 50 mA/cm² is 1.711. It is slightly different of the case of one single layer because of the presence of the thin barrier [22]. The refractive index of the cladding layer prepared by applying a current density of 100 mA/cm² is 1.475.

These parameters were chosen because the difference in contrast between the guiding layer and the cladding layer is sufficiently high ($\Delta n = 0.236$) to satisfy light propagation conditions, and because the pore size of the guiding layer is large enough to allow efficient infiltration of the target, and small enough to avoid light scattering.

After the photolithography process, the ridge waveguide is designed with particular dimensions (width of 6 µm and thickness of 2.3 µm for the guiding layer) originally targeted to allow single-mode light propagation according to a simulation calculation performed ~~using FIMWAVE software~~ using a FMM (Film Mode Matching) which is a full vector solver from a commercial software (FIMMWAVE, Photon Design). The FMM solver [37] is a versatile numerical method for vector mode-field calculations and is ideally suited to a rectangular waveguide geometry as well as ridge waveguide structures used in this study.

~~The PSi-based waveguide enabling an external confinement factor Γ_{TM} = 115 % at λ = 4.23 µm for the fundamental TM mode, with the evanescent power factor for the superstrate (air) is equal to 8.63 %, and the power factor of guiding layer and cladding layer is equal to 55.22 % and 36.15 % respectively.~~

The external confinement factor expressed in equation (8) [2], is defined as the sensitivity of the waveguide to complex refractive index variation in the active sensing region:

$$\Gamma = \frac{\partial n_{eff}}{\partial n_{superstrat}} = \frac{n_g}{n_{superstrate}} \frac{\iint_{superstrat} \varepsilon \left|\vec{E}\right|^2 dx\, dy}{\iint_{\infty} \varepsilon \left|\vec{E}\right|^2 dx\, dy} \qquad (8)$$

Where n_{eff} is the effective refractive index, $n_{superstrate}$ the sensing active area refractive index, n_g is the group index, ε the permittivity and $\vec{E}$ the electric field.

The PSi-based waveguide enabling an external confinement factor estimated at Γ_{TM} = 115 % and Γ_{TE} = 111 % at λ = 4.23 µm for the fundamental TM and TE modes, respectively. Since the propagated light was randomly polarized as we use a fiber to couple the light into the waveguide, the value of Γ should take a value between Γ_{TE} and Γ_{TM}.

Otherwise, in the case of a waveguide based on porous materials, the external confinement factor surpasses the unity value (100 %) because light interacts not only with target molecules on the surface, but also with those inside the waveguide, as well as inside the superstrate, guiding and cladding layers. This important interaction thus causes a sensitivity enhancement. An external confinement factor Γ greater than unity has been already demonstrated by using the equation (8) [38-40].

The propagation losses of the ridge waveguide as a function of the oxidation treatment at the mid-IR were measured using the "cut-back" method (Figure 9-a). Light propagation losses measurements for this ridge waveguide were performed in the wavelength range of 3.90 to 4.35 µm. We note that the oxidation treatment was carried out after the etching process and on the same waveguide (sample).

The graphs in Figure 9-a show that the optical loss curves increase with oxidation treatment and wavelength due to the absorption of silica, and their increase with wavelength, as shown in Figure 9-b. Silica absorption was calculated according to the optical loss equations (9). With ~~A~~ $\alpha_{material}(\mathrm{cm}^{-1}) = 4\pi k(n)/\lambda(\mathrm{cm})$ is the absorption coefficient; $k(n)$, the imaginary part of the complex refractive index and λ, the wavelength in cm.

$$\alpha\ (\mathrm{dB/cm}) = \frac{10\ \text{~~A~~}\ \alpha_{material}(\mathrm{cm}^{-1})}{\ln(10)} \qquad (9)$$

The optical losses of the as-prepared ridge waveguide in the wavelength range of 3.95 to 4.30 µm is about 10 dB/cm (green curve; circle-shaped). ~~These losses values result from surface and volume scattering, due to surface roughness and nanostructure respectively.~~ These loss values result mainly from free carrier absorption in the heavily doped bulk silicon substrate, which are estimated to be in the range of 4 and 400 cm^{-1} in the case of bulk materials for the wavelength of 4 µm [41]. The optical

losses also increase below 3.95 µm and above 4.30 µm wavelengths due to the absorption of Si-OH and Si-H [28]. After one hour of pre-oxidation at 300 °C, a thin film of silica formed on the porous surface layers, resulting in a high increase in optical losses as a function of wavelength, following the silica absorption curve (Figure 9-b). The presence of this thin silica film also results in a decrease in spectral transmission region for propagation (blue curve; square -shaped). Then, the propagation losses increase dramatically after partial oxidation to about 60 dB/cm (pink curve; triangle-shaped), due to the increase of the silica component in the waveguide. It should be noted that the large optical losses error found after partial oxidation is due to the insufficient number of points to measure, and the propagation losses below 3.94 µm wavelength have not been taken into account, because the waveguide output signal was very low (close to the noise level), making the propagation loss extraction generate overestimated values. Finally, after full oxidation, the ridge waveguide became based on porous silica layers. And so, no propagation is observed in the mid-IR region through the fully oxidized waveguide, as the silica completely absorbs the propagated light. Only propagated light in the near-IR (at 1.55 µm) was observed through the ridge waveguide after the full oxidation.

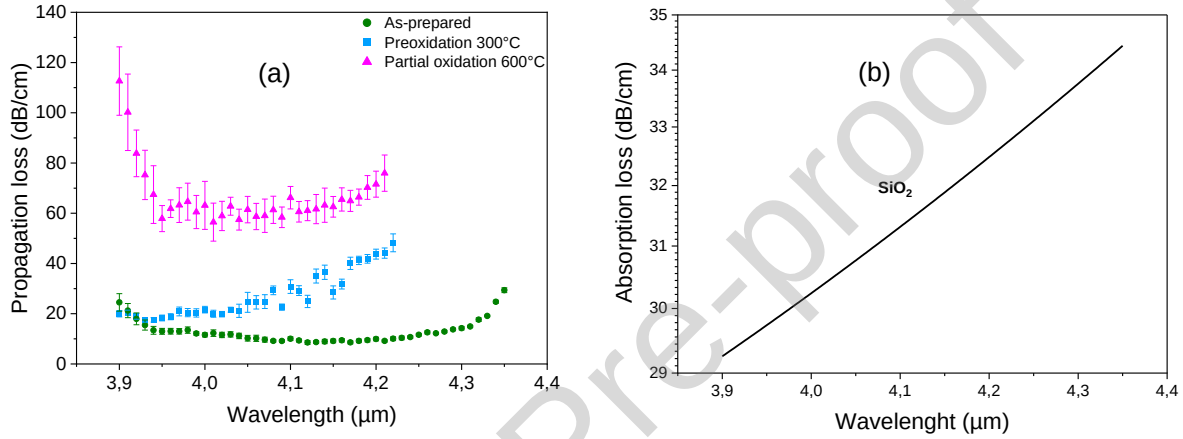

Figure 9: (a) Propagation optical losses for a ridge waveguide as a function of oxidation treatment. (b) Absorption loss of silica at mid-IR (3.90 - 4.35 µm).

The sensitivity of the ridge waveguide based on PSi layers has been calculated for CO_2 gas detection in the mid-IR at 4.23 µm wavelength. Sensitivity S is defined by the variation in output optical power P as a function of the concentration C of the target molecules according to equation (10).

$$S = \left|\frac{dP}{dC}\right| = \varepsilon \, \eta \, \Gamma \, L \, P \qquad (10)$$

Where, $P = P_0 \exp\left(-\varepsilon \, \eta \, \Gamma \, C \, L - \alpha_{prop} \, L\right)$ is the optical power transmitted through the waveguide according to the Lambert-Beer's law [42, 43], P_0 (W) the optical power at the waveguide input, C (mol.L^{-1}) the concentration of the target molecules, ε the molar absorption which is equal to 2613 L.cm^{-1}.mol^{-1} for CO_2 gas at around 4.3 µm wavelength [44], η Γ (%) the external confinement factor, L (cm) the waveguide length and α_{prop} (cm^{-1}) the waveguide propagation optical loss.
The sensitivity of the integrated sensor based on the PSi waveguide with 0.57 cm length is equal to 2.85 ± 0.05 W.(L.mol^{-1}) for a CO_2 gas concentration of 1000 ppm (4.10^{-5} mol.L^{-1}) [45], taking into account the following parameters: P_0 = 7 mW, ~~η = 115 %~~ Γ takes a value between 111 % and 115 % and $\alpha_{prop} = 2.35$ cm^{-1}.

Conclusions

In this paper, PSi layers were developed by electrochemical anodization and then oxidized by heat treatment in air at different temperatures. This study was performed in the mid-infrared spectral range. The effect of the oxidation treatment on the porous structure of the PSi single layers has been introduced. The porosity of PSi layers decreases with heat treatment due to the insertion of oxygen

atoms into the silicon crystallites. The problematic issues of oxidation treatment on the optical properties of the PSi layers have been investigated. The oxidation treatment gradually reduces the transparency of the PSi layer from 8 µm to 5 µm wavelength until complete oxidation, due to the high absorption of silica in this medium. A ridge waveguide based on PSi layers (bilayer) has been designed by a photolithography process. This waveguide is capable of transmitting light in the mid-IR spectral range at a wavelength around 4.3 µm, both before and after undergoing partial oxidation at 600°C. The propagation losses of the ridge waveguide was measured in the mid-IR (3.90 - 4.35 µm). The results showed an increase in losses before and after partial oxidation from 10 to 60 dB/cm at a wavelength of around 4.1 µm, due to the increased transformation of silicon to silica. ~~Despite the absorption of silica in the mid-IR, we consider that an optical waveguide made of oxidized PSi remains very sensitive and has a low detection limit. This is due to the porous structure of the waveguide, which offers a large interaction surface between the transmitted light and the analytes.~~ However, an optical waveguide based on porous silicon materials represents a new generation of integrated transducers operating in the mid-infrared range, which is considered a new challenge in future sensing applications. This type of transducer is highly sensitive despite the high optical losses compared with a waveguide based on bulk materials [17, 46].

Funding

Thanks to Lannion Trégor Communauté (LTC) and Conseil Général des Côtes d'Armor (CD22) for funding the doctoral thesis of the PhD JAAFAR Abdallah.

This work was supported by the French national research agency under MID-VOC ANR project (ANR-17-CE09-0028-01) and Projet Hubert Curien under PHC Maghreb project (07MAG21). Equipment funding of Institut Foton were partly provided by the CPER Sophie.

Acknowledgments

Scanning Electron Microscopy imaging and porous silicon fabrication were performed in the CCLO - Rénatech + technological platform of Institut Foton.

References

[1] A. Yadav and A. M. Agarwal, "Integrated photonic materials for the mid-infrared," *Int J Appl Glass Sci*, vol. 11, no. 3, pp. 491–510, Jul. 2020, doi: 10.1111/ijag.15252.

[2] D. M. Kita, J. Michon, S. G. Johnson, and J. Hu, "Are slot and sub-wavelength grating waveguides better than strip waveguides for sensing?," *Optica*, vol. 5, no. 9, p. 1046, Sep. 2018, doi: 10.1364/OPTICA.5.001046.

[3] N. L. Kazanskiy, S. N. Khonina, and M. A. Butt, "Advancement in Silicon Integrated Photonics Technologies for Sensing Applications in Near-Infrared and Mid-Infrared Region: A Review," *Photonics*, vol. 9, no. 5, p. 331, May 2022, doi: 10.3390/photonics9050331.

[4] T. Hu *et al.*, "Silicon photonic platforms for mid-infrared applications [Invited]," *Photon. Res.*, vol. 5, no. 5, p. 417, Oct. 2017, doi: 10.1364/PRJ.5.000417.

[5] Julian Haas, Erhan Tütüncü, Andreas Wilk, Vjekoslav Kokoric, and Boris Mizaikoff, "Next-Generation Mid-Infrared Chemical and Biological Sensors: Combining Quantum Cascade Lasers with Thin-Film and Hollow Waveguides." Jan. 2017.

[6] G. Z. Mashanovich *et al.*, "Low loss silicon waveguides for the mid-infrared," *Opt. Express*, vol. 19, no. 8, p. 7112, Apr. 2011, doi: 10.1364/OE.19.007112.

[7] DAYLIGHT-SOLUTIONS, “Région du MIR. Représentation graphique de la localisationdans le MIR des molécules d’intérêt avec des forts absorptions.” [Online]. Available: http://www.daylightsolutions.com/technology/qcl_technology.htm.
[8] P. Granitzer and K. Rumpf, “Metal Filled Nanostructured Silicon With Respect to Magnetic and Optical Properties,” *Front. Phys.*, vol. 8, p. 121, Apr. 2020, doi: 10.3389/fphy.2020.00121.
[9] S. Lee, J. Kang, and D. Kim, “A Mini Review: Recent Advances in Surface Modification of Porous Silicon,” *Materials*, vol. 11, no. 12, p. 2557, Dec. 2018, doi: 10.3390/ma11122557.
[10] R. Vercauteren, G. Scheen, J.-P. Raskin, and L. A. Francis, “Porous silicon membranes and their applications: Recent advances,” *Sensors and Actuators A: Physical*, vol. 318, p. 112486, Feb. 2021, doi: 10.1016/j.sna.2020.112486.
[11] M. K. Sahoo and P. Kale, “Restructured porous silicon for solar photovoltaic: A review,” *Microporous and Mesoporous Materials*, vol. 289, p. 109619, Nov. 2019, doi: 10.1016/j.micromeso.2019.109619.
[12] R. Moretta, L. De Stefano, M. Terracciano, and I. Rea, “Porous Silicon Optical Devices: Recent Advances in Biosensing Applications,” *Sensors*, vol. 21, no. 4, p. 1336, Feb. 2021, doi: 10.3390/s21041336.
[13] L. Canham, *Handbook of porous silicon*, 2nd ed. Springer:Switzerland, 2018.
[14] V. P. Bondarenko, A. M. Dorofeev, and N. M. Kazuchits, “Optical waveguide based on oxidized porous silicon,” *Microelectronic Engineering*, vol. 28, no. 1–4, pp. 447–450, Jun. 1995, doi: 10.1016/0167-9317(95)00094-O.
[15] A. Loni *et al.*, “Porous silicon multilayer optical waveguides,” *Thin Solid Films*, vol. 276, no. 1–2, pp. 143–146, Apr. 1996, doi: 10.1016/0040-6090(95)08075-9.
[16] P. Pirasteh, J. Charrier, Y. Dumeige, P. Joubert, S. Haesaert, and L. Haji, “Further results on porous silicon optical waveguides at 1.55 μm,” *Physica Status Solidi (a)*, vol. 204, no. 5, pp. 1346–1350, May 2007, doi: 10.1002/pssa.200674333.
[17] P. Girault *et al.*, “Porous silicon micro-resonator implemented by standard photolithography process for sensing application,” *Optical Materials*, vol. 72, pp. 596–601, Oct. 2017, doi: 10.1016/j.optmat.2017.07.005.
[18] P. Azuelos *et al.*, “Optimization of porous silicon waveguide design for micro-ring resonator sensing applications,” *J. Opt.*, vol. 20, no. 8, p. 085301, Aug. 2018, doi: 10.1088/2040-8986/aad01b.
[19] F. O. Briano, C. Errando-Herranz, and K. B. Gylfason, “On-Chip Dispersion Spectroscopy of CO2 Using a Mid-Infrared Microring Resonator,” in *Conference on Lasers and Electro-Optics*, Washington, DC: Optica Publishing Group, 2020, p. STh1N.3. doi: 10.1364/CLEO_SI.2020.STh1N.3.
[20] C. Ranacher *et al.*, “Mid-infrared absorption gas sensing using a silicon strip waveguide,” *Sensors and Actuators A: Physical*, vol. 277, pp. 117–123, Jul. 2018, doi: 10.1016/j.sna.2018.05.013.
[21] T. Jin, J. Zhou, and P. T. Lin, “Real-time and non-destructive hydrocarbon gas sensing using mid-infrared integrated photonic circuits,” *RSC Adv.*, vol. 10, no. 13, pp. 7452–7459, 2020, doi: 10.1039/C9RA10058J.
[22] F. Cassio *et al.*, “Porosity calibration in a 4-layer porous silicon structure to fabricate a micro-resonator with well-defined refractive indices and dedicated to biosensing applications,” *Optical Materials*, vol. 110, p. 110468, Dec. 2020, doi: 10.1016/j.optmat.2020.110468.
[23] M. Morita, T. Ohmi, E. Hasegawa, M. Kawakami, and M. Ohwada, “Growth of native oxide on a silicon surface,” *Journal of Applied Physics*, vol. 68, no. 3, pp. 1272–1281, Aug. 1990, doi: 10.1063/1.347181.
[24] J. J. Yon, K. Barla, R. Herino, and G. Bomchil, “The kinetics and mechanism of oxide layer formation from porous silicon formed on *p* -Si substrates,” *Journal of Applied Physics*, vol. 62, no. 3, pp. 1042–1048, Aug. 1987, doi: 10.1063/1.339761.
[25] A. E. Pap *et al.*, “Thermal oxidation of porous silicon: Study on structure,” *Appl. Phys. Lett.*, vol. 86, no. 4, p. 041501, Jan. 2005, doi: 10.1063/1.1853519.
[26] D. A. G. Bruggeman, “Berechnung verschiedener physikalischer Konstanten von heterogenen Substanzen. I. Dielektrizitätskonstanten und Leitfähigkeiten der Mischkörper aus isotropen Substanzen,” *Ann. Phys.*, vol. 416, no. 7, pp. 636–664, 1935, doi: 10.1002/andp.19354160705.
[27] R. Herino, A. Perio, K. Barla, and G. Bomchil, “Microstructure of Porous silicon and its evolution with temperature,” *Materials Letters*, vol. 2, no. 6, pp. 519–523, Sep. 1984, doi: 10.1016/0167-577X(84)90086-7.
[28] J. Salonen, V.-P. Lehto, and E. Laine, “Thermal oxidation of free-standing porous silicon films,” *Appl. Phys. Lett.*, vol. 70, no. 5, pp. 637–639, Feb. 1997, doi: 10.1063/1.118294.

[29] P. Girault, “Micro-résonateurs intégrés pour des applications capteurs.” PhD thesis, Université Rennes 1, 2016.
[30] K. Barla, R. Herino, and G. Bomchil, “Stress in oxidized porous silicon layers,” *Journal of Applied Physics*, vol. 59, no. 2, pp. 439–441, Jan. 1986, doi: 10.1063/1.337036.
[31] N. Lorrain *et al.*, “Submicron gap reduction of micro-resonator based on porous silica ridge waveguides manufactured by standard photolithographic process,” *Optical Materials*, vol. 88, pp. 210–217, Feb. 2019, doi: 10.1016/j.optmat.2018.11.038.
[32] J. Fletcher, G. Parish, J. Dell, and A. Keating, “Morphological and Optical Transformation of Gas Assisted Direct Laser Written Porous Silicon Films,” *Small*, p. 2300655, Apr. 2023, doi: 10.1002/smll.202300655.
[33] D. S. Bethune, “Optical harmonic generation and mixing in multilayer media: analysis using optical transfer matrix techniques,” *J. Opt. Soc. Am. B*, vol. 6, no. 5, p. 910, May 1989, doi: 10.1364/JOSAB.6.000910.
[34] N. Lorrain, M. Hiraoui, M. Guendouz, and L. Haji, “Functionalization control of porous silicon optical structures using reflectance spectra modeling for biosensing applications,” *Materials Science and Engineering: B*, vol. 176, no. 14, pp. 1047–1053, Aug. 2011, doi: 10.1016/j.mseb.2011.05.040.
[35] Salzberg and Villa, “Optical constants of Si (Silicon) : : n 1.36–11 µm.” 1957.
[36] Kischkat et al., “Optical constants of SiO2 (Silicon dioxide, Silica, Quartz) : Thin film; n,k 1.54–14.3 µm.” 2012.
[37] A. S. Sudbo, “Film mode matching: a versatile numerical method for vector mode field calculations in dielectric waveguides,” *Pure Appl. Opt.*, vol. 2, no. 3, pp. 211–233, May 1993, doi: 10.1088/0963-9659/2/3/007.
[38] M. Vlk *et al.*, “Extraordinary evanescent field confinement waveguide sensor for mid-infrared trace gas spectroscopy,” *Light Sci Appl*, vol. 10, no. 1, p. 26, Jan. 2021, doi: 10.1038/s41377-021-00470-4.
[39] C. Consani, F. Dubois, and G. Auböck, “Figures of merit for mid-IR evanescent-wave absorption sensors and their simulation by FEM methods,” *Opt. Express*, vol. 29, no. 7, p. 9723, Mar. 2021, doi: 10.1364/OE.415825.
[40] G. J. Veldhuis, O. Parriaux, H. J. W. M. Hoekstra, and P. V. Lambeck, “Sensitivity Enhancement in Evanescent Optical Waveguide Sensors,” *J. Lightwave Technol.*, pp. 18, 677, 2000.
[41] D. K. Schroder, R. N. Thomas, and J. C. Swartz, “Free carrier absorption in silicon,” *IEEE Trans. Electron Devices*, vol. 25, no. 2, pp. 254–261, Feb. 1978, doi: 10.1109/T-ED.1978.19066.
[42] J. Charrier *et al.*, “Evanescent wave optical micro-sensor based on chalcogenide glass,” *Sensors and Actuators B: Chemical*, vol. 173, pp. 468–476, Oct. 2012, doi: 10.1016/j.snb.2012.07.056.
[43] A. Gutierrez-Arroyo *et al.*, “Optical characterization at 7.7 µm of an integrated platform based on chalcogenide waveguides for sensing applications in the mid-infrared,” *Opt. Express*, vol. 24, no. 20, p. 23109, Oct. 2016, doi: 10.1364/OE.24.023109.
[44] A. Gutierrez-Arroyo *et al.*, “Theoretical study of an evanescent optical integrated sensor for multipurpose detection of gases and liquids in the Mid-Infrared,” *Sensors and Actuators B: Chemical*, vol. 242, pp. 842–848, Apr. 2017, doi: 10.1016/j.snb.2016.09.174.
[45] M. Laska and E. Dudkiewicz, “Research of CO_2 concentration in naturally ventilated lecture room,” *E3S Web Conf.*, vol. 22, p. 00099, 2017, doi: 10.1051/e3sconf/20172200099.
[46] P. Girault *et al.*, “Integrated polymer micro-ring resonators for optical sensing applications,” *Journal of Applied Physics*, vol. 117, no. 10, p. 104504, Mar. 2015, doi: 10.1063/1.4914308.

Declaration of interests

The authors declare that they have no known competing financial interests or personal relationships that could have appeared to influence the work reported in this paper.

Highlights

- Integrated sensor based on porous silicon (PSi) ridge waveguide in the Mid-infrared spectral range
- Optical characterizations and estimation of optical losses in the Mid Infrared range around 4 µm
- Study of the effect of oxidation of PSi on the optical losses in the Mid Infrared range around 4 µm